LRP 565/96 December 1996

PARTICLE-IN-CELL (PIC) SIMULATIONS OF BEAM INSTABILITIES IN GYROTRONS

T.M. Tran, G. Jost, K. Appert, S. Alberti,
M. Pedrozzi

Submitted for publication in
Physics of Plasmas

Particle-In-Cell (PIC) Simulations of Beam Instabilities in Gyrotrons

T.M. Tran, G. Jost, K. Appert, S. Alberti, M. Pedrozzi

CRPP, Association Euratom-Confédération Suisse

Ecole Polytechnique Fédérale de Lausanne, Switzerland.

Abstract

Extensive simulations are performed to investigate effects of electron cyclotron instabilities on the gyrotron beam quality, using two-dimensional axisymmetric particle-in-cell (PIC) codes. Both electrostatic and electromagnetic models, as well as realistic geometries of the gyrotron are considered. It is found that a large beam density can lead to an electrostatic-instability-induced energy spread which substantially degrades the gyrotron efficiency.

41.75.Ht, 52.35.Qz, 52.65.Rr, 84.40.Ik

I. INTRODUCTION

One of the main prerequisites for efficient operation of high power microwave sources, such as the gyrotron and the free-electron-laser, is the good quality of the electron beams. For gyrotrons in particular, the velocity spreads may affect the beam coupling to the electromagnetic wave. The beam energy spread is important as well, since the energy extraction efficiency depends strongly on the detuning parameter $\delta = 1 - \Omega_{ce}/\gamma\omega$ where Ω_{ce} is the non-relativistic electron cyclotron frequency, γ the electron relativistic factor and ω the wave frequency. In general, beam optics can only induce velocity spreads, producing an almost mono-energetic beam, since the energy spread induced by the DC space charge across the thin beam is negligible. This is also the case when considering the effects of the surface roughness of the gun emitter. On the other hand, beam instabilities which can occur in the beam tunnel, can induce *both* velocity and energy spreads, and thus could deteriorate the beam and its interaction with the microwave in the resonator. On the basis of single-mode calculations, a substantial reduction of the gyrotron efficiency has been predicted in [1] due to an energy spread $\Delta\gamma/\gamma$ as small as 1% and less.

Beam diagnostics have been employed recently to measure the beam velocity distribution in gyrotrons. They are based on the *retarding potential* technique [2] and the *electron cyclotron emission* [1]. Both methods provide only the parallel velocity distribution and assume a *mono-energetic* beam in order to estimate the perpendicular velocity distribution.

In the present paper, numerical simulations using the Particle-In-Cell (PIC) method are presented to study the electron beam instabilities occurring close to the electron cyclotron frequency Ω_{ce}/γ. The principal focus is the determination of the various spreads mentioned above, induced by the instabilities in realistic conditions (geometry, external magnetic profile). Both electrostatic and electromagnetic models are considered. These types of simulations have already been considered in 1D [3] and in 2D [4] in the context of electrostatic noise amplification in gyrotron amplifiers.

In sec. II, the PIC simulation models are described in detail. The linear theory of

the electrostatic electron cyclotron instability for a uniform plasma and perfectly aligned gyrocenter beam is briefly reviewed and compared to the 1D PIC simulations in sec. III. The 2D electrostatic and electromagnetic simulation results are presented in section IV and V respectively and finally the section VI contains some concluding remarks.

II. PIC SIMULATION MODELS

The simulation model assumes that the beam electron dynamics is fully relativistic. The equations of motion of the particles are thus written as

$$\frac{d\vec{u}}{dt} = \frac{q}{m}\left[\vec{E}(\vec{x},t) + \frac{\vec{u}\times\vec{B}(\vec{x},t)}{\gamma}\right], \qquad \frac{d\vec{x}}{dt} = \frac{\vec{u}}{\gamma}. \tag{1}$$

where $\vec{u} = \gamma\vec{v}$ is the particle momentum, $\gamma = \sqrt{1+u^2/c^2}$ is the relativistic factor, m and q are respectively the mass and the charge of the simulation particle and c is the velocity of light.

In the *electrostatic* approximation, the electric field is expressed in terms of an electric potential $\vec{E} = -\nabla\phi$ and $\vec{B}$ is a static magnetic field imposed externally. $\vec{B}(x)$ can, for example, be computed from a set of coils, using the Biot-Savart equations. Each particle is pushed using Eq. (1) which is time-discretized by the usual second order *leapfrog* scheme [5,6]. Using the axisymmetry of the geometry and cylindrical coordinates in which the azimuthal coordinate θ is an ignorable variable, the particle phase space coordinates are $(\vec{x},\vec{u}) = (r,z,u_r,u_\theta,u_z)$ and the charge density can be constructed from the ensemble of N_p electrons as

$$\rho(r,z,t) = q\sum_{p=1}^{N_p}\frac{\delta(r-r_p(t))}{2\pi r}\delta(z-z_p(t)). \tag{2}$$

The variational form of the Poisson equation, using the charge density as defined by Eq. (2), is then

$$\iint_\Omega \nabla\psi\cdot\nabla\phi\, r dr dz = \frac{q}{2\pi\epsilon_0}\sum_{p=1}^{N_p}\psi(r_p(t),z_p(t)), \tag{3}$$

where the integration is performed over the 2D computational domain Ω, and ψ is an arbitrary weight function from the same function space as ϕ. The Finite Element discretization of the Poisson equation is then completely defined by choosing the *bilinear* basis functions ψ_i, $i = 1, \ldots, N$ on a (r, z) mesh of N grid points [7]. The discretized potential can thus be expressed as $\phi(r, z, t) = \sum_{i=1}^{N} \phi_i(t)\psi_i(r, z)$, where the coefficients $\phi_i(t)$ are obtained by solving the following linear matrix equation:

$$\sum_{j=1}^{N} A_{ij}\phi_j(t) = Q_i(t)/\epsilon_0, \tag{4a}$$

$$A_{ij} = \iint \nabla\psi_i \cdot \nabla\psi_j \, r dr dz, \quad Q_i(t) = \frac{q}{2\pi} \sum_{p=1}^{N_p} \psi_i(r_p(t), z_p(t)). \tag{4b}$$

Dirichlet boundary conditions, $\phi = \text{const.}$, are specified on perfectly conducting walls by modifying the matrix A_{ij} and the charges Q_i in a standard manner. Natural boundary conditions (normal derivative $\partial\phi/\partial n = 0$) are automatically included in the matrix formulation above. The latter conditions are utilized for the field at the symmetry axis $r = 0$ and to model the open sides of the boundaries. The electric field at the particle position is finally calculated from $\vec{E}(r, z, t) = -\sum_{i=1}^{N} \phi_i(t)\vec{\nabla}\psi_i(r, z)$. Noe that, by the choice of the bilinear basis functions ψ_i, the charge deposited on the grid Q_i, as defined in Eq. (4b), is computed by an linear assignment, while the electric field interpolation on the particle is stepwise constant (linear) in r and linear (constant) in z for E_r (E_z). This scheme is similar to the *energy-conserving* scheme described in [5].

At every simulation time step, the beam is continuously injected at the left end of the computational domain, $z = 0$, with a prescribed constant current I, a given number of injected particles N_{inj} and a distribution function of guiding centers $F_{inj}(r_g, u_\perp, u_{||}, \varphi)$, where $u_\perp, u_{||}$ are respectively the momenta perpendicular and parallel to $\vec{B}$, $u_{||} > 0$ and F is uniform in the pitch angles φ. Finite spreads in the guiding center radius r_g as well as in the velocities $u_\perp, u_{||}$ can be prescribed. The charge of these particles is given by $q = -I\Delta t/N_{inj}$ while their mass m is such that the charge to mass ratio is that of an electron $q/m = -e/m_e$. At both ends of the domain, free boundary conditions are applied for particles with $u_z < 0$

at $z = 0$ and $u_z > 0$ at $z = L_z$. The total number of particles N_p is thus a time varying function with $N_p(t = 0) = 0$. It increases linearly with time up to approximately one transit of the beam electrons across the computational domain.

Electrons of a non-drifting plasma could also be simulated together with the beam electrons. The simulated charge of these N_{sim} plasma electrons is then $q = -eN_{plasma}/N_{sim}$, where $N_{plasma} = \int n_0 dV$ and n_0 is the constant plasma density. At both ends of the domain, either periodic or reflecting boundary conditions are applied to these plasma electrons so as to keep N_{sim} constant.

The equations (1) and (4) form a complete electrostatic model for the self-consistent evolution of the electron beam. It has been implemented on a massively parallel computer, using the domain decomposition technique to parallelize the particles as well as the electrostatic field. The parallel direct matrix solver described in [8] is utilized for solving the discretized Poisson equation (4).

The extension of this model to include electromagnetic effects consists of solving the Maxwell equations for the fields $\vec{E}(\vec{r}, t)$ and $\vec{B}(\vec{r}, t)$. In the axisymmetric case considered here, the electromagnetic fields can be decomposed into the decoupled TM polarization (E_r, E_z, B_θ) and the TE polarization (B_r, B_z, E_θ). The particle equations (1) remain unchanged but the current density has to be calculated:

$$\vec{J}(r, z, t) = q \sum_{p=1}^{N_p} \vec{v}_p(t) \frac{\delta(r - r_p(t))}{2\pi r} \delta(z - z_p(t)). \tag{5}$$

The detailed description of this electromagnetic model and its implementation is given in [9].

III. REVIEW OF LINEAR RESULTS

The linear theory has been used by several authors to analyze the electrostatic electron cyclotron instability. In [3], Chu considered a neutral, uniform and infinite plasma approximation. Assuming an uniform external magnetic field $B_0\vec{e}_z$ and a cold electron

beam, represented by the distribution $F = \delta(u_\perp - u_{\perp 0})\,\delta(u_\parallel - u_{\parallel 0})/(2\pi u_\perp)$, he found an approximated linear growth rate for the n^{th} cyclotron harmonic, $\omega \simeq n\Omega_{ce}/\gamma$, given by

$$\omega_i = \frac{nJ_n(k_x r_L)}{k_x r_L}\,\frac{\beta_{\perp 0}}{\sqrt{\gamma}_0}\,\omega_{pe}, \tag{6}$$

where Ω_{ce}, ω_{pe} are the *non-relativistic* electron cyclotron and plasma frequency respectively, $r_L = u_{\perp 0}/\Omega_{ce}$ is the Larmor radius, $\beta_{\perp 0}$ is the initial perpendicular velocity normalized to the velocity of light c, $\gamma_0 = (1 + u_{\perp 0}^2/c^2 + u_{\parallel 0}^2/c^2)^{1/2}$ is the initial relativistic factor, k_x is the perpendicular component of the wave vector and J_n is the n^{th} order of the Bessel function.

The more elaborate model of a perfectly aligned gyrocenter beam has been considered in [10,11]. The electron density across the magnetic field of such a beam, assuming that it is cold and centered at $x = 0$, has the following dependence

$$n_e(x) = \frac{2\overline{n_e}}{\pi}\,\frac{1}{\sqrt{1 - x^2/r_L^2}}, \tag{7}$$

where $\overline{n_e}$ is the beam density averaged over the beam diameter $2r_L$. The growth rate at the n^{th} cyclotron harmonic is then

$$\omega_i = \frac{1}{\pi}\sqrt{\frac{2n^2}{n^2 - 1/4}}\,\frac{\beta_{\perp 0}}{\sqrt{\gamma}_0}\,\overline{\omega_{pe}}, \tag{8}$$

where $\overline{\omega_{pe}}$ is the averaged non-relativistic plasma frequency. Notice that both growth rates as given in Eqs. (6) and (8) exhibit the same dependence in the perpendicular velocity $\beta_{\perp 0}$ and the density, together with a weak decrease for increasing harmonic numbers n.

A one dimensional electrostatic simulation can readily be done for the model used in the analytical results presented above, by considering a slab with the Cartesian phase space coordinates (x, u_x, u_y) of Eq. (1). The matrix A_{ij} and the charge array $Q_i(t)$ of the discretized Poisson equation (4a) now simplify to

$$A_{ij} = \int \psi_i'(x)\psi_j'(x)\,dx, \quad Q_i(t) = \frac{q}{S_{yz}}\sum_{p=1}^{N_p}\psi_i(x_p(t)), \tag{9}$$

where S_{yz} is the area of the simulated beam slab. The simulation starts by loading a cold and perfectly-aligned guiding-center electron distribution. A small perturbation $\delta\varphi_p = \epsilon\sin(n\varphi_p)$

is then imposed on the uniformly distributed gyro-angles φ_p, to excite the n^{th} cyclotron harmonic mode. The growth rates calculated from the 1D slab simulation are compared to the analytical predictions in Fig. 1, showing good agreement, especially in the low density region: the small discrepancy can be attributed to the low density assumption used to obtain Eq. (8). For high harmonic numbers, the simulation growth rates are slightly smaller than the theoretical estimates, as can be seen in Fig. 2.

IV. 2D ELECTROSTATIC SIMULATIONS

Let us first consider a simple cylinder of constant radius $R_w = 5$ mm. The Dirichlet boundary condition (perfectly conducting wall) is applied at $r = R_w$ and Neumann conditions are assumed at both ends, $z = 0$ and $z = L_z$. A cold annular electron beam with a pitch angle $\alpha \equiv u_\perp/u_{||} = 1.5$ and energy $V_0 = 70$ kV is injected at $z = 0$ into the cylinder, immersed in an uniform magnetic field $\vec{B} = B_0\vec{e}_z$. This geometry can be considered as the simplest model for the beam tunnel connecting the gun region to the gyrotron resonator. The simulation starts from noise and, for a given beam current I, the tunnel length L_z is chosen sufficient for saturation to take place before the beam enters the resonator. A quasi-steady state is reached after about three electron transit times along the cylinder. Typical longitudinal profiles of spreads at this state are illustrated in Fig. 3, showing the convective nature of the instability. By performing a time Fourier analysis of the potential along the axis, $\phi(r = 0, z, t)$, after the quasi steady-state has been reached, it can be seen that the instabilities occur, indeed, at frequencies close to the relativistic electron cyclotron frequency $\omega_{ce} = \Omega_{ce}/\gamma$ (see Fig. 4). The Fourier transform in z of this signal, displayed in Fig. 5, clearly shows that, in addition to the Doppler shifted electron cyclotron branch $\omega = \pm\omega_{ce} + k_z v_z$, the low frequency Langmuir wave $\omega = \pm\omega_{pe} + k_z v_z \simeq k_z v_z$ has also been excited.

In Fig. 6, the saturated velocity and energy spreads are displayed versus the beam density. For each value of the beam density, the system length L_z is chosen sufficiently large to reach

saturation. The results from the 1D simulation described above are also reported in figure. 6, showing that the 2D spreads are only slightly larger than the 1D ones: the finite Doppler shift $k_z v_z$ does not seems to be an important effect for the electrostatic instability with uniform B. In most gyrotrons, the beam density $\omega_{pe}^2/\Omega_{ce}^2$ is usually smaller than 10^{-2} since high current beams are designed to also have large cross-sections. As a consequence, the maximum perpendicular velocity spread due to the electrostatic electron cyclotron instability is expected to be around 10%. However, the spreads in γ can be as large as 1% which exceeds by at least an order of magnitude what can be expected from DC space charge effects alone. As shown in Ref. [1], such values of $\Delta\gamma/\gamma$ could significantly reduce the gyrotron interaction efficiency. In order to assert that the instability can occur in the beam tunnel, and hence degrade the beam quality before reaching the gyrotron resonator, it is important to consider the effects of non-uniform magnetic fields in the beam tunnel.

In Ref. [4], the effects of the magnetic field gradient have been considered using a linear magnetic taper. It was shown that the nonlinear saturated spreads are not affected even though the linear amplification rates k_i can change (see Fig. 5 of [4]). This change is due to the increase (decrease) of the density and $\beta_\perp$ in a positive (negative) magnetic field taper, consistent with the linear growth rate given in Eq. (8).

In the following, we will use the real magnetic field found in two existing gyrotrons: the first (gyrotron I) is a quasi-optical gyrotron operating at 90 GHz [12] and the second (gyrotron II) is a cylindrical cavity gyrotron operating at 118 GHz [13]. Experimental measurements have shown that the quasi-optical gyrotron efficiency saturates at a maximum value of 15% instead of the predicted 22%, while in the second device, the measured efficiencies agree well with the theory prediction. In the simulation, we consider only the beam tunnel extending from the end of the acceleration region to the center of the resonator, as shown in Fig. 7. The magnetic field for both cases is computed from the gyrotron coils. The phase space distribution of the injected beam is specified using the equilibrium obtained from the electron gun design code Daphne [14].

The steady state frequency spectra of the electrostatic potential ϕ at $r = 0$, in the case

of gyrotron I, are plotted at different axial positions in Fig. 8, revealing that electrostatic instabilities are developed at frequencies close to the *local* electron cyclotron frequency $\omega_{ce}(z)$. As in the uniform B case, a weak excitation at low frequencies could also be observed.

The evolution of the computed energy spreads, displayed in Fig. 7, shows that the maximum spreads in gyrotron I are much larger than those in gyrotron II. In addition, the instability developed in gyrotron II is not yet saturated, due to the shorter beam tunnel. The main cause of the larger spreads found in gyrotron I is, however, the larger beam density reached in the maximum magnetic compression region as can be inferred from Fig.9. Notice that the correlation between the maximum spread $\Delta\gamma/\gamma$ and the normalized beam density $\omega_{pe}^2/\Omega_{ce0}^2$ (with Ω_{ce0} calculated using the maximum B field) is practically the same as that found in the constant magnetic field case, shown in Fig. 6. We thus get the simple result that gyrotron II has smaller energy spreads because the beam was designed to have a small density. Referring to the calculations of the efficiency versus the energy spread shown in Fig. 12 of [1], the efficiency in gyrotron I is expected to decrease to 18% from its monoenergetic beam prediction of 22%; while in gyrotron II, the effects of the spreadsinduced by the electrostatic instability should remain negligible on the efficiency.

The space charge depression induced by an opening in the quasi-optical gyrotron is simulated, using the geometry illustrated in Fig. 10. In order to single out the effect of the beam depression, the external magnetic field is assumed uniform. The simulated domain is 20 cm long with an opening of 12 cm located at its center. A $\alpha = 1.5$ and $V = 70$ kV cold annular beam is injected at the left side. The steady state velocity and energy spreads calculated at the right boundary are shown versus the beam current in Fig. 11. By comparing these spreads with those obtained without beam depression (see e.g. Fig. 6), it is clear that the space charge depression has no effect on the electrostatic instability.

Finally, the presence of a background plasma is considered by adding a population of non-drifting cold electrons in the simulation with a specified density. These cold electrons could roughly model an imperfect vacuum in the gyrotron or the secondary electrons which can be emitted by the gyrotron walls. We have observed no noticeable effects on the instability,

except when the background electron density largely exceeds the beam density. In that case, a strong two-stream instability occurs, drastically changing the phase space distribution of the beam electrons.

V. 2D ELECTROMAGNETIC SIMULATIONS

The main goal of the electromagnetic simulations is to find whether the electromagnetic perturbations have an effect on the beam electrostatic instability, thus increasing the degradation of the beam quality. A detailed investigation, using the full electromagnetic model, has been conducted and presented in [9]: only the essential physical results of this investigation are summarized below.

As expected, backward TE and TM waves can easily be excited in the lossless cylinders considered here, leading to large spreads of the perpendicular velocity $\Delta u_\perp/u_\perp$. The parallel velocity spreads $\Delta u_{||}/u_{||}$ however are comparable to those found in the electrostatic case. In addition, the electrostatic perturbations can be identified in the electromagnetic simulations, but do not seem to be affected by the electromagnetic perturbations.

Electromagnetic simulations with a magnetic taper have been performed as well, showing that the magnetic gradient can suppress the electromagnetic instability when the excited frequency is not close to the cut-off ($k_z \simeq 0$). For the particular case of the gyrotron shown in Fig. 7a, it is found that the magnetic field gradient in the beam tunnel impedes the excitation of the backward waves.

Although the electromagnetic perturbations can induce very large values of $\Delta u_\perp/u_\perp$, they can easily be suppressed in the beam tunnel by introducing absorbers on the wall and/or by tapering the wall, unlike the electrostatic perturbations.

VI. CONCLUSION

A 2D axisymmetric PIC code has been developed to investigate the adverse effects of the electron cyclotron instabilities on the electron beam quality in the gyrotron. Both

electrostatic and electromagnetic interactions are considered. The main result is that the electrostatic instability can induce energy spreads, of an order of magnitude larger than can be expected from beam optics, and can thus lead to degradation of the gyrotron efficiency.

The large beam density was identified as the main cause for large energy spreads, which can be quickly estimated using Fig. 6. In high power gyrotrons which usually operate at high current, and high frequency quasi-optical gyrotrons in which the beam cross-section should be kept small in order to couple efficiently with the standing wave of the Fabry-Perrot resonator, the beam density should, indeed, be kept small. However, this may be difficult to achieve.

ACKNOWLEDGMENTS

This work was supported in part by the Swiss National Science Foundation and by Cray Research, Inc. within the framework of the Cray Research/EPFL Parallel Application Technology Program. The computations were performed on the Cray T3D massively parallel computer at EPFL, Lausanne. The authors would like to acknowledge O. Sauter, S. Wuthrich and S. Merazzi for their help during the code development, T. Goodman for reading the manuscript and M.Q. Tran for very fruitful discussions.

REFERENCES

[1] G. Soumagne *et al.*, Phys. Plasmas **3**, 3501 (1996).

[2] B. Piosczyk, in *Proc. 18th Int. conference on infrared and millimeter waves, Colchester*, edited by J. R. Birch and T. J. Parker (SPIE, Washington, 1993), pp. 450–451.

[3] K. R. Chu and L. H. Lyu, IEEE Trans. Microwave Theory Tech. **34**, 690 (1986).

[4] F. S. Kuo and K. R. Chu, Chinese J. of Phys. **28**, 327 (1990).

[5] C. K. Birdsall and A. B. Langdon, *Plasma Physics via Computer Simulation* (McGraw-Hill Inc., New-York, 1985).

[6] R. W. Hockney and J. W. Eastwood, *Computer Simulation using Particles* (Adam Hilger Inc., Bristol and Philadelphia, 1988).

[7] G. Strang and G. Fix, *An Analysis of the Finite Element Method* (Prentice-Hall, Inc, Englewood Cliffs, N.J., 1973).

[8] T. M. Tran, R. Gruber, K. Appert, and S. Wuthrich, Comp. Phys. Comm. **96**, 118 (1996).

[9] G. Jost, T. M. Tran, K. Appert, and S. Wuthrich, accepted for publication in Comp. Phys. Comm.

[10] A. Bondeson and T. M. Antonsen, Int. J. Electron. **61**, 855 (1986).

[11] V. L. Bratman and A. V. Savilov, Phys. Plasmas **2**, 557 (1995).

[12] J. P. Hogge, T. M. Tran, P. J. Paris, and M. Q. Tran, Phys. Plasmas **3**, 3492 (1996).

[13] E. Giguet *et al.*, in *Proc. Twentieth Int. conference on infrared and millimeter waves, Orlando*, edited by R. Temkin, pp. 339–340.

[14] T. M. Tran, D. R. Whaley, and R. G. S. Merazzi, in *Proc. 6th joint EPS-APS Int. Conf. on Physics Comput.* (EPS, Geneva, Swizerland, 1994), p. 492.

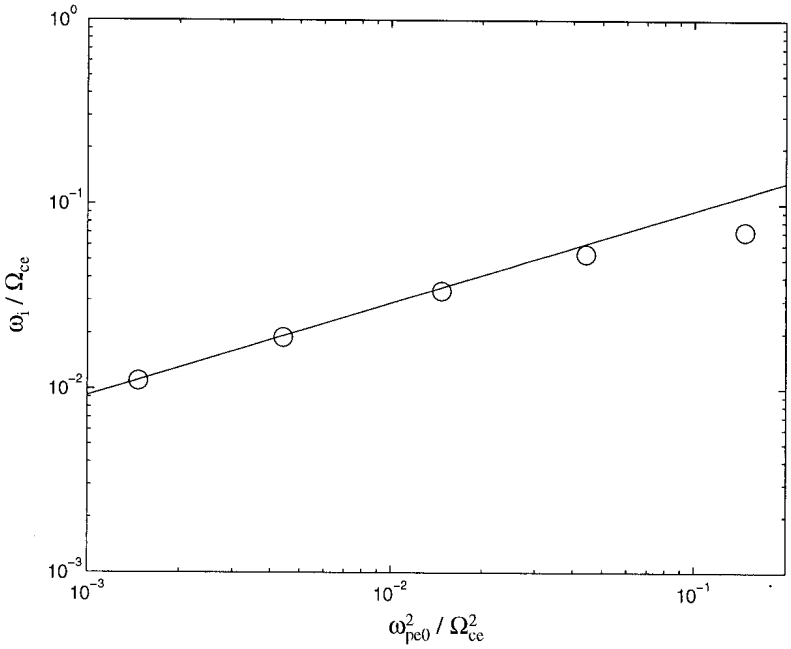

FIG. 1. Comparison of linear growth rates obtained from 1D simulations (◯) and linear theory (continuous line) for $V_0 = 70$ kV and $\beta_z = 0$.

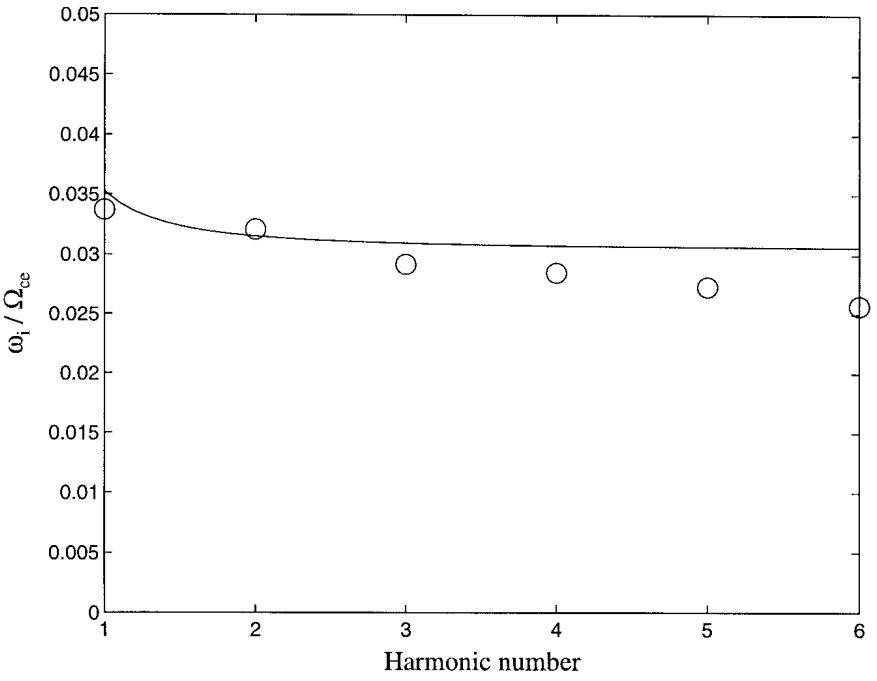

FIG. 2. Linear growth rates versus harmonic numbers obtained from 1D simulations (◯) and linear theory (continuous line) for $V_0 = 70$ kV, $\beta_z = 0$ and $\omega^2_{pe0}/\Omega^2_{ce} = 0.0147$.

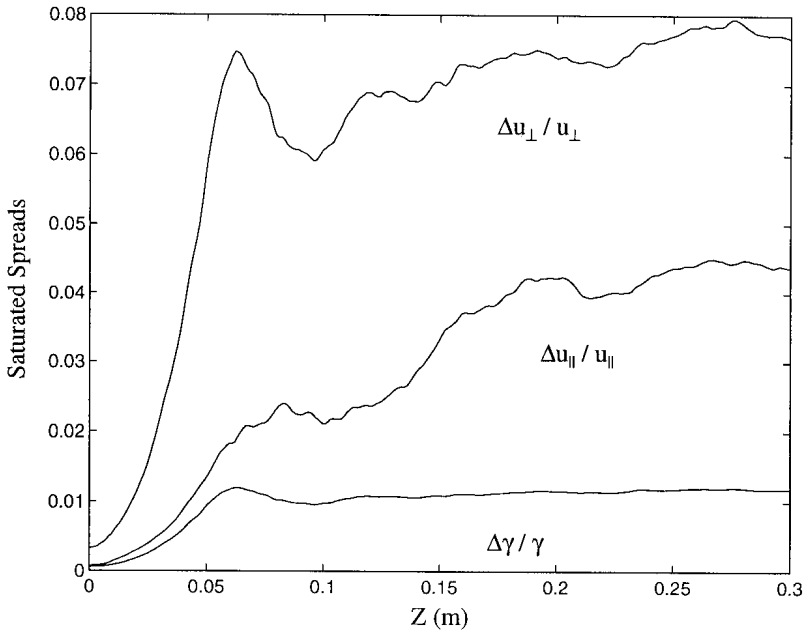

FIG. 3. Profiles of $\Delta u_\perp/u_\perp$ (top curve), $\Delta u_{||}/u_{||}$ (middle curve) and $\Delta\gamma/\gamma$ (bottom curve), at saturation for $I = 40$ A, $V_0 = 70$ kV and $\alpha = 1.5$.

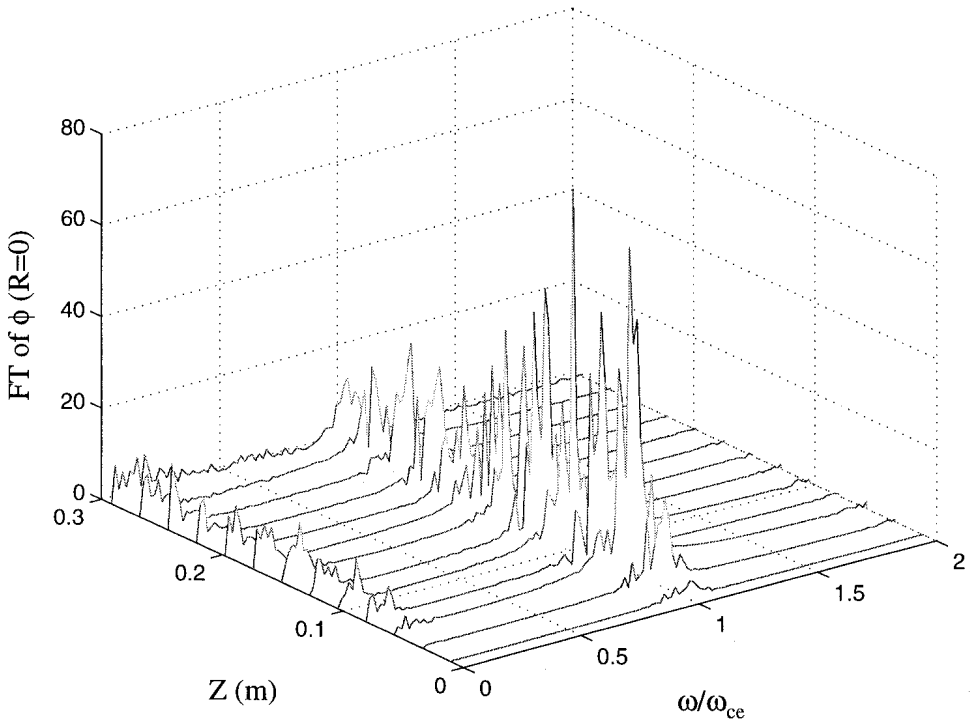

FIG. 4. The steady state frequency spectrum of the electrostatic potential at the axis $R = 0$ for $I = 40$ A, $V_0 = 70$ kV and $\alpha = 1.5$.

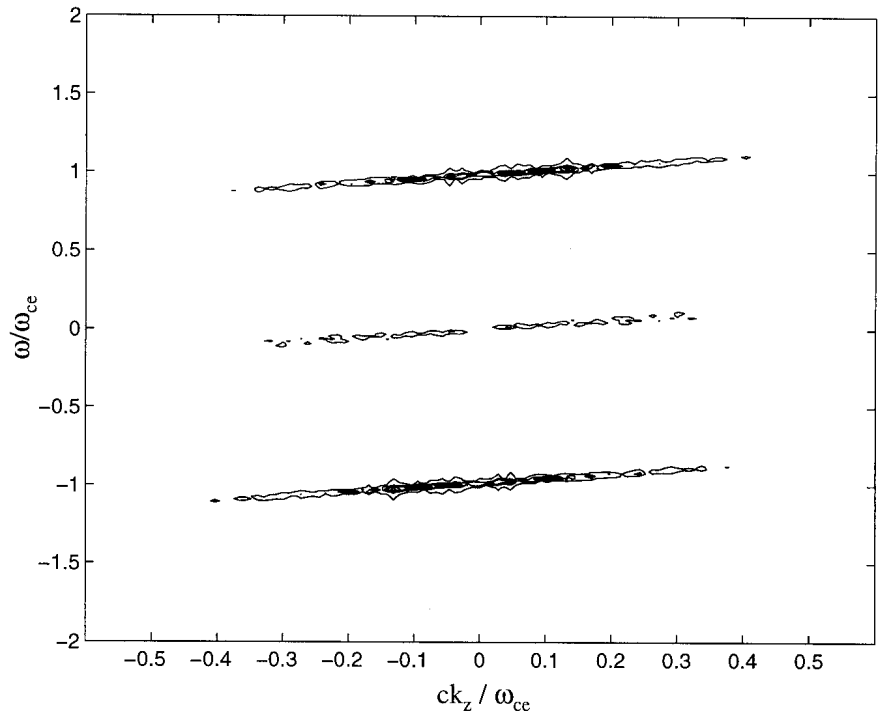

FIG. 5. The time and space Fourier transform of the electrostatic potential at the axis $R = 0$ for $I = 40$ A, $V_0 = 70$ kV and $\alpha = 1.5$.

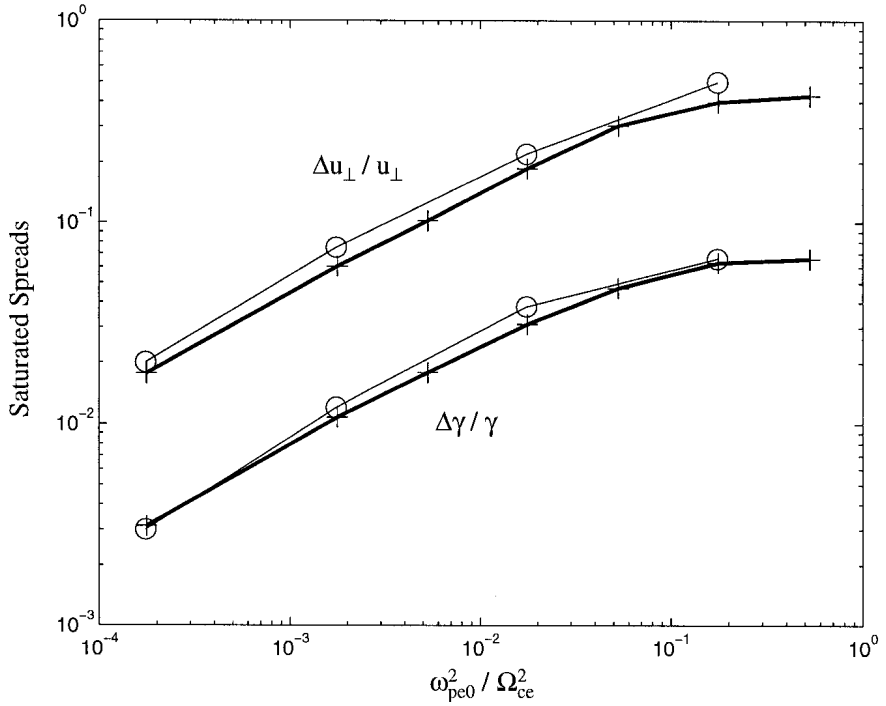

FIG. 6. Comparison of saturated perpendicular velocity (upper curves) and energy (lower curves) spreads obtained from 1D (+) and 2D (◯) simulations for $V_0 = 70$ kV and $\alpha = 1.5$.

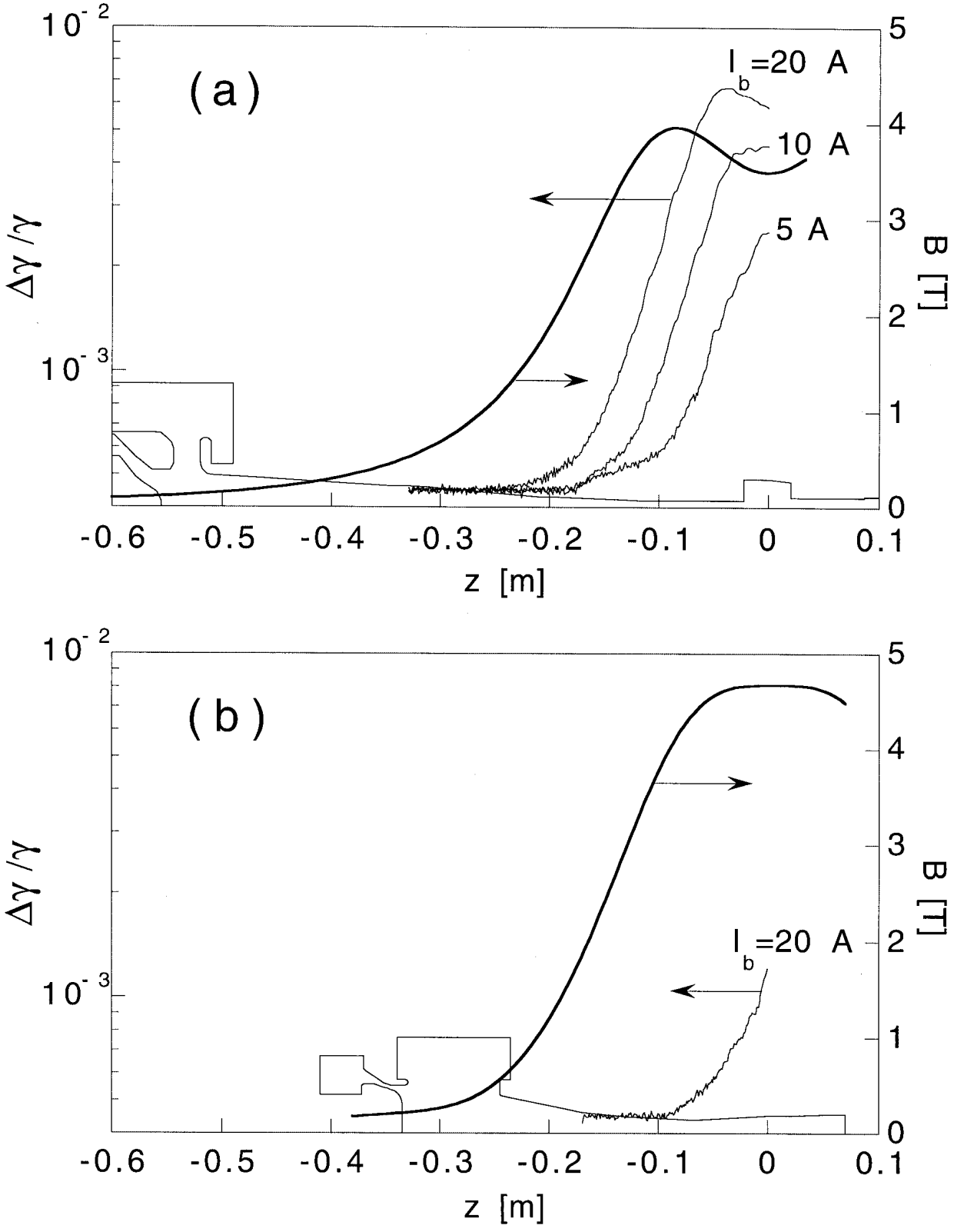

FIG. 7. Profiles of the saturated spreads in gyrotron I (a) and II (b). The origin of the z axis is chosen to be at the center of the resonator. Only the beam tunnel is considered in the simulation of the electrostatic instability.

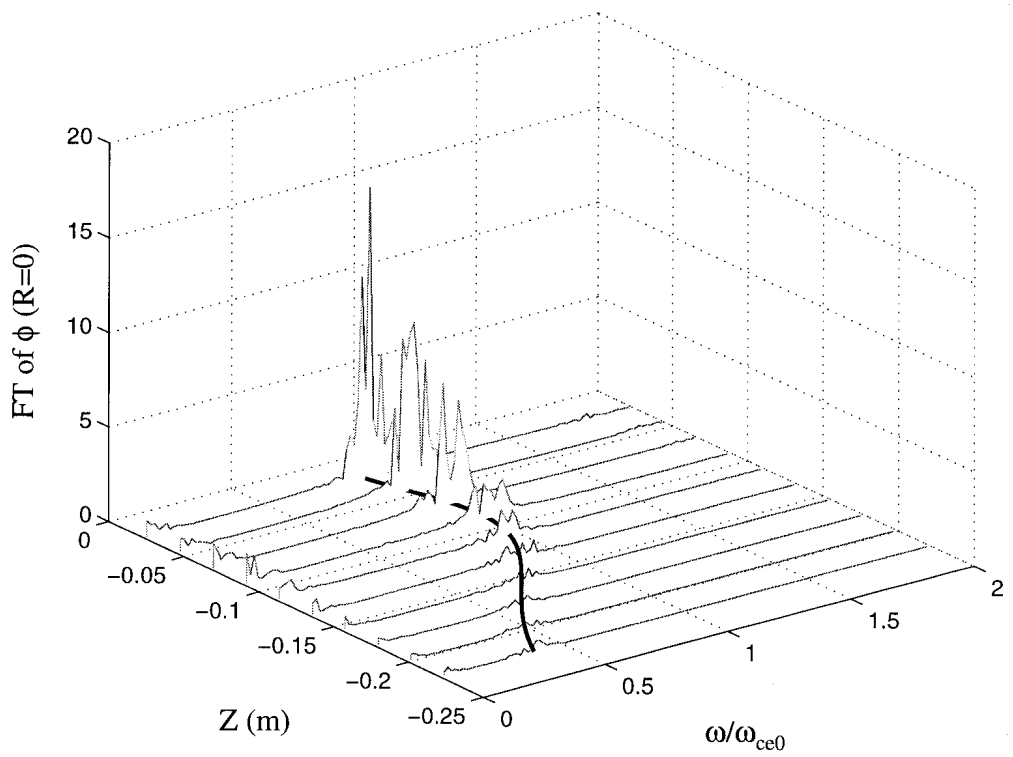

FIG. 8. The steady state frequency spectrum of the electrostatic potential at the axis $R = 0$ for gyrotron I with $I = 10$ A. The profile of the local electron cyclotron frequency $\omega_{ce}(z)/\omega_{ce0}$ is represented by a thick line on the horizontal plane.

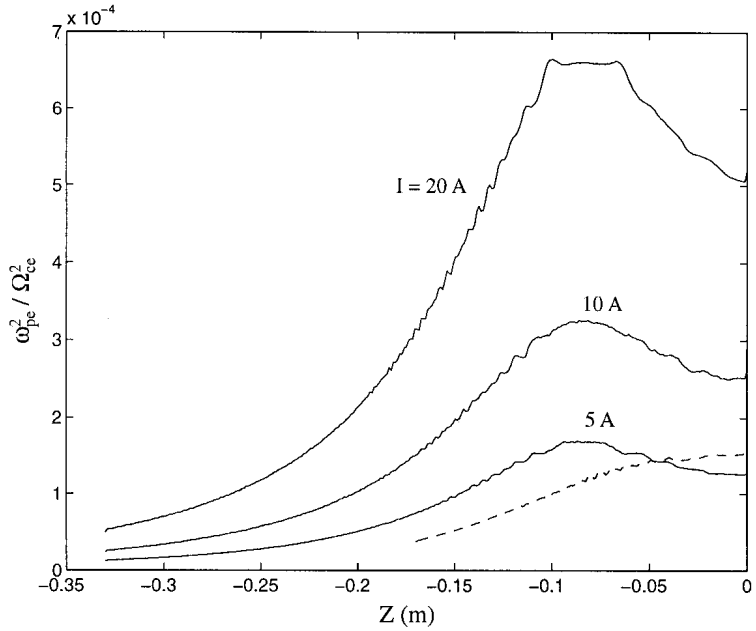

FIG. 9. Profiles of the normalized density $\omega_{pe}^2/\Omega_{ce}^2$ in gyrotron I (solid line) for several beam currents and gyrotron II (dashed line) for $I = 20$ A.

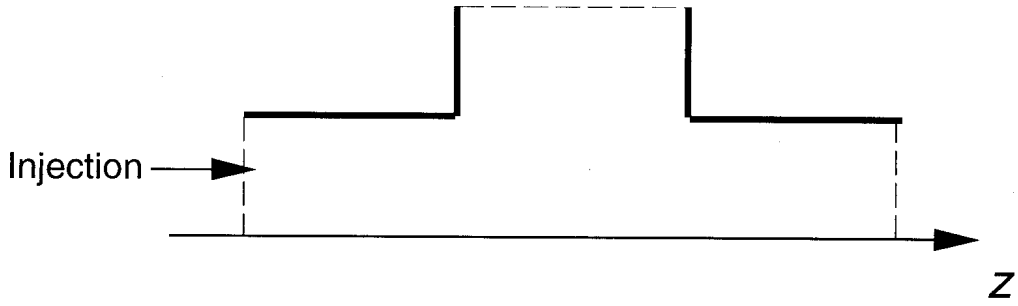

FIG. 10. The geometry considered in the simulation: the Dirichlet boundary condition is applied to the cavity wall (thick lines) while the Neumann condition is assumed on the open boundaries (dashed lines).

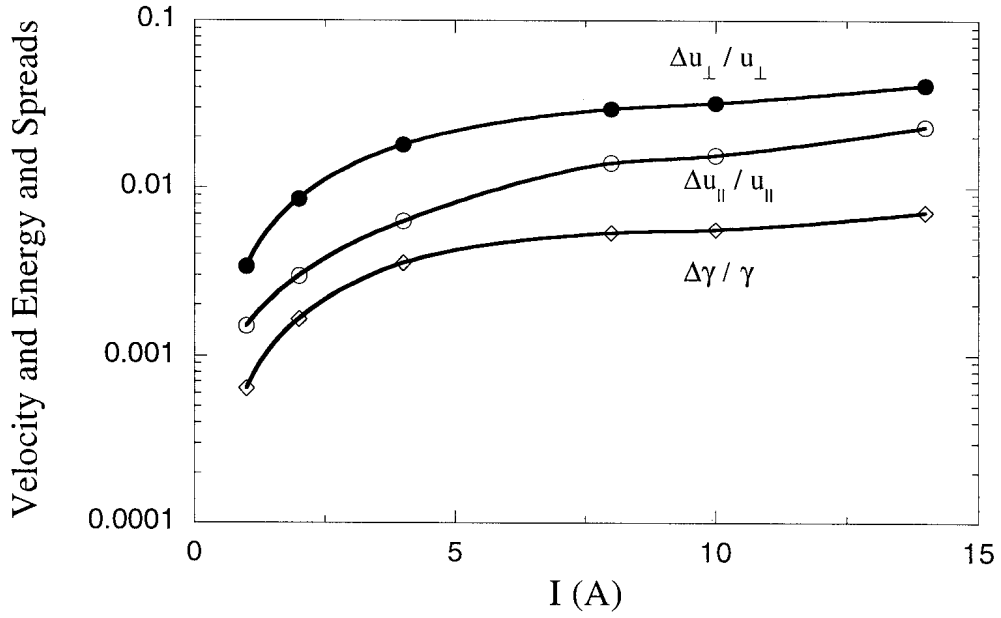

FIG. 11. The saturated spreads versus the beam current I for the case shown in Fig. 10